Molecular Dynamics and NMR Spectroscopy Studies of *E. coli* Lipopolysaccharide Structure and Dynamics

Emilia L. Wu,[†△] Olof Engström,[‡△] Sunhwan Jo,[†] Danielle Stuhlsatz,[†] Min Sun Yeom,[§] Jeffery B. Klauda,[¶] Göran Widmalm,[‡*] and Wonpil Im[†*]

[†]Department of Molecular Biosciences and Center for Bioinformatics, The University of Kansas, Lawrence, Kansas; [‡]Department of Organic Chemistry and Stockholm Center for Biomembrane Research, Arrhenius Laboratory, Stockholm University, Stockholm, Sweden; [§]Korean Institute of Science and Technology Information, Yuseong-gu, Daejeon, Korea; and [¶]Department of Chemical and Biomolecular Engineering, The University of Maryland, College Park, Maryland

ABSTRACT Lipopolysaccharide (LPS), a component of Gram-negative bacterial outer membranes, comprises three regions: lipid A, core oligosaccharide, and O-antigen polysaccharide. Using the CHARMM36 lipid and carbohydrate force fields, we have constructed a model of an *Escherichia coli* R1 (core) O6 (antigen) LPS molecule. Several all-atom bilayers are built and simulated with lipid A only (LIPA) and varying lengths of 0 (LPS0), 5 (LPS5), and 10 (LPS10) O6 antigen repeating units; a single unit of O6 antigen contains five sugar residues. From ^{1}H,^{1}H-NOESY experiments, cross-relaxation rates are obtained from an O-antigen polysaccharide sample. Although some experimental deviations are due to spin-diffusion, the remaining effective proton-proton distances show generally very good agreement between NMR experiments and molecular dynamics simulations. The simulation results show that increasing the LPS molecular length has an impact on LPS structure and dynamics and also on LPS bilayer properties. Terminal residues in a LPS bilayer are more flexible and extended along the membrane normal. As the core and O-antigen are added, per-lipid area increases and lipid bilayer order decreases. In addition, results from mixed LPS0/5 and LPS0/10 bilayer simulations show that the LPS O-antigen conformations at a higher concentration of LPS5 and LPS10 are more orthogonal to the membrane and less flexible. The O-antigen concentration of mixed LPS bilayers does not have a significant effect on per-lipid area and hydrophobic thickness. Analysis of ion and water penetration shows that water molecules can penetrate inside the inner core region, and hydration is critical to maintain the integrity of the bilayer structure.

INTRODUCTION

The cytoplasm of Gram-negative bacteria is surrounded by a cell envelope, which consists of the inner membrane, the periplasm, and the outer membrane. The inner membrane is a lipid bilayer composed of phospholipids and integral membrane proteins with α-helical transmembrane domains. The periplasm is a viscous compartment located between the inner and outer membranes (1,2). The outer membrane is a unique and highly asymmetric lipid bilayer composed of phospholipids in the inner leaflet and mostly lipopolysaccharides (LPSs) in the outer leaflet (3–8). It also contains integral membrane proteins with β-barrel structures, such as porins and gated channels (9). The outer membrane separates the periplasm from the external environment and serves as a protective barrier that controls the entry of many toxic molecules such as antibiotics and bile salts into the bacteria, which is crucial for bacterial survival in diverse/hostile environments (2,10).

LPSs are vital to both the structural integrity and the function of the Gram-negative bacteria (11) and composed of lipid A, a core oligosaccharide, and an O-antigen polysaccharide with various lengths of repeating units (Fig. 1 *A*) (1,12,13). Lipid A (endotoxin) causes severe biological effects in mammals, such as fever and septic shock (13). It anchors LPS molecules in the outer membrane and functions as the scaffold for assembly of the core and the O-antigen (14). Lipid A is composed of a glucosamine dimer bound to lipid acyl chains that can vary in length and number depending on the bacterial strains and environment (15). Covalently linked to lipid A is the core portion of the molecule, which can be further divided into the inner and outer cores. The inner core is proximal to lipid A and contains a high proportion of rare sugars such as 2-keto-3-deoxyoctulosonate (Kdo) and L-glycero-D-manno-heptose (Hep). The outer core extends further from lipid A and consists of common sugars such as hexoses and hexosamines (11). The core oligosaccharide and lipid A are negatively charged, resulting in strong affinity for divalent cations. This strong ionic interaction is crucial for bilayer integrity and membrane function (16). Attached to the outer core is the O-antigen, a polymer of repeating saccharide units with 3–6 monosaccharides arranged into linear or branched structures; sometimes the latter has more than one branch, which makes the three-dimensional structure highly complex (11). The composition and structure of the O-antigen polysaccharide varies according to the serological group. Currently, there are over 190 identified O-serotypes for *Escherichia coli* (17), whereas there are only five known core structures (R1–R4 and K12) and lipid A is highly conserved (11,18,19).

E. coli is the most common cause of food poisoning and urinary tract infections, and it is also responsible for many

Submitted May 17, 2013, and accepted for publication August 1, 2013.

△Emilia L. Wu and Olof Engström contributed equally to this work.

*Correspondence: wonpil@ku.edu or gw@organ.su.se

Editor: Reinhard Lipowsky.

0006-3495/13/09/1444/12 $2.00

http://dx.doi.org/10.1016/j.bpj.2013.08.002

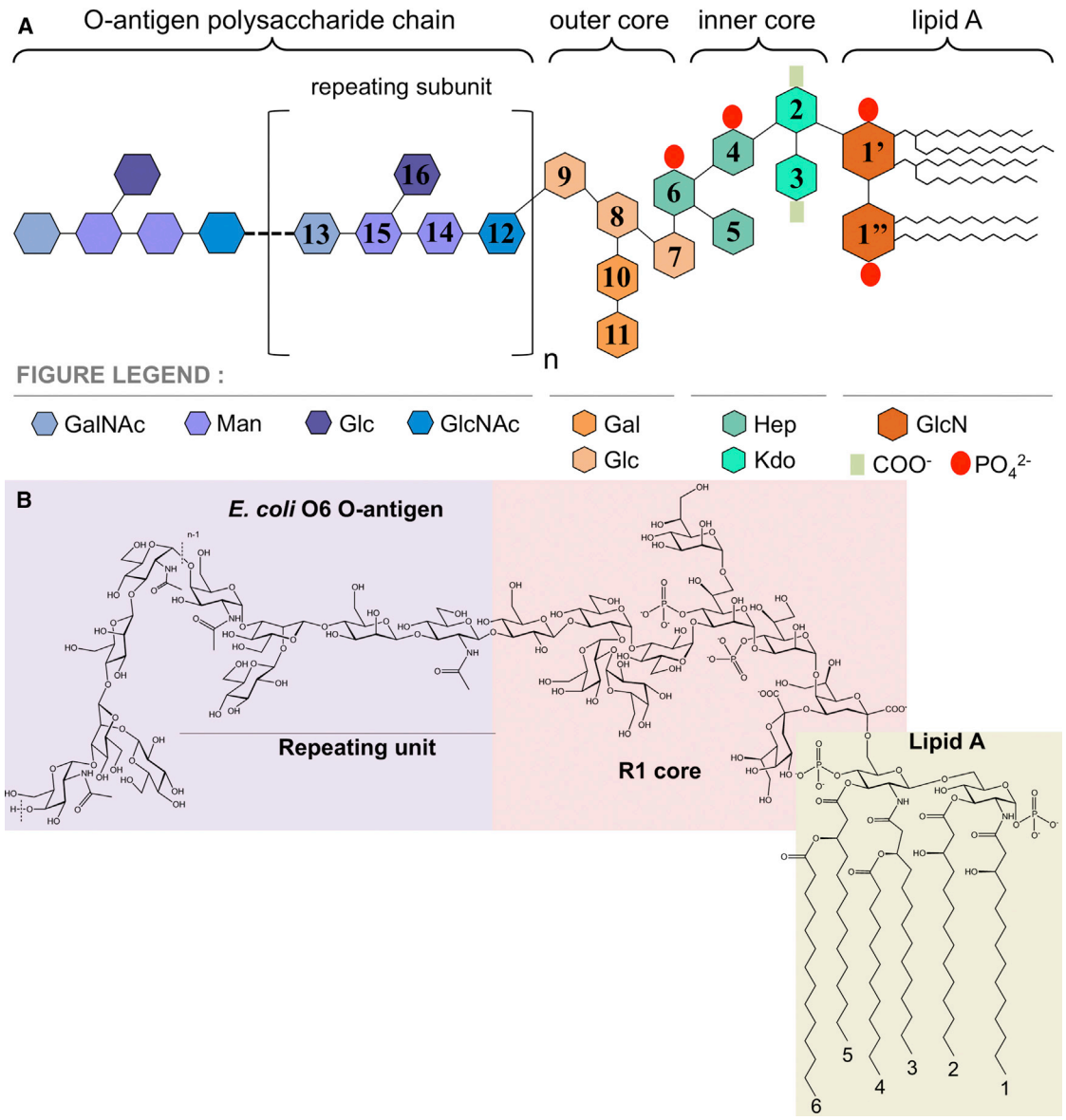

FIGURE 1 (*A*) A schematic representation of *E. coli* R1 O6 LPS structure (Kdo: 2-keto-3-deoxyoctulosonate; Hep: L-glycero-D-manno heptose; Man: D-mannose; Glc: D-glucose; Gal: D-galactose; GlcN: D-glucosamine; GlcNAc: *N*-acetyl-D-glucosamine; GalNAc: *N*-acetyl-D-galactosamine), modified based on Erridge et al.'s work (11), and (*B*) its chemical structure. The numbers in (*A*) are the residue numbers used in this study. The lipid A of *E. coli* LPS consists of two D-glucosamine residues joined by a β-(1→6)-linkage, two monophosphoester groups at O1 and O4′, and six amide/ester-linked fatty acids. The *E. coli* R1 core (most common core type reported for *E. coli* (83)) has two Kdo residues and three Hep residues, two of which have a monophosphoester group at their O4 position in the inner core. Nonstoichiometric decoration with ethanolamine or glucosamine may also occur in this region, but is not considered in this study. The outer core consists of five hexopyranoses, three D-glucoses, and two D-galactoses, all of which are α-linked, except for the β-linkage between the last two glucose residues. The O6 antigen polysaccharide is attached to the O3 position of the terminal glucosyl residue in the outer core and its linkage has the β-configuration. This is in contrast to the corresponding α-(1→4)-linkage between the repeating units. Access to the semirough strain (i.e., containing only one O-antigen repeating unit) also facilitated determination of the biological repeating unit with a 3-substituted *N*-acetyl-D-glucosamine residue at the reducing end (19). The additional sugars in the repeating unit are two β-D-mannoses, one *N*-acetyl-α-D-galactosamine, leading to four sugars in the backbone of the polymer, and a β-D-glucose residue forming a branched structure via its (1→2)-linkage to the second mannose residue.

gastrointestinal diseases such as travelers' and infantile diarrhea (11,20). Interestingly, the LPS of *E. coli* alone can be the causative agent for a number of diseases by activating the mammalian immune system and stimulating host responses (11). To better understand the LPS recognition by the immune system and its biological function in their native environment, it is necessary to obtain information on LPS structure and dynamics at the molecular level. In this work, using the CHARMM36 (C36) lipid and carbohydrate (21–26) force fields, the three-dimensional structure of *E. coli* R1 (core) O6 (antigen) LPS was built based on its primary structure (sugar and lipid components, substituents,

anomeric configurations, ring forms, substitution positions, and sequence of sugars) from the previous chemical and spectroscopic studies (Fig. 1 and Table S1 in the Supporting Material) (19,27). We then performed molecular dynamics (MD) simulations of four homogeneous explicit LPS bilayers based on *E. coli* R1 O6 LPS molecule: with lipid A only (LIPA) and the core region added (LPS0), having 5 (LPS5), and having 10 (LPS10) O6 antigen repeating units. These simulations provide insights into the impact of molecular length on structure and dynamics of LPS molecules in a bilayer and LPS bilayer properties. We also constructed and simulated four heterogeneous LPS bilayers with different lengths of O-antigens mixed (LPS0/LPS5 and LPS0/LPS10), which allows us to further explore the influence of the O-antigen chain heterogeneity on molecular structure and dynamics as well as bilayer properties. In addition, ^{1}H,^{1}H-NOESY NMR experiments on an *E. coli* O6 antigen polysaccharide sample were performed to compare with and validate the MD simulations of these LPS bilayers.

METHODS

MD simulations

We assembled four LPS bilayers with different LPS lengths. For simplicity, they are denoted as LIPA (lipid A), LPS0 (lipid A + R1 core), LPS5 (lipid A + R1 core + 5 repeating units of O6 antigen), and LPS10 (lipid A + R1 core + 10 repeating units of O6 antigen) (Fig. 2 and Fig. S1). The LPS

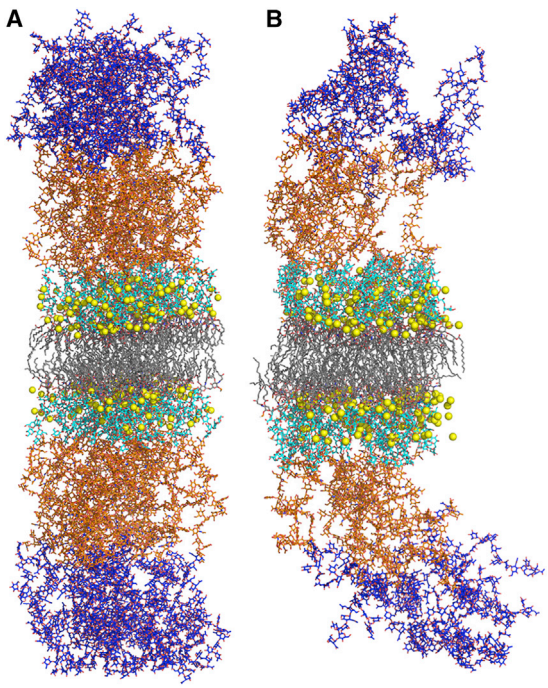

FIGURE 2 LPS lipid bilayer snapshots: (*A*) LPS10 (lipid A + R1 core + 10 units of O6 antigen) and (*B*) MIX10_50 (LPS0/LPS10 mixed bilayer with 50% LPS10). The coordinate sets are from the 100-ns time point. Lipid A, R1 core, O6 antigen repeating units 1–5, and repeating units 6–10 are colored in gray, cyan, orange, and blue, respectively. Calcium ions are shown in yellow spheres. Water molecules and KCl are not shown for clarity.

membrane building and simulation procedures have been generalized in the following five steps, and all the input files including LPS molecule building together with all the relevant topology and parameter files are provided in the Supporting Material (lps.tar). The force field parameters of new residues (Lipid A, HEP, KDO) were manually assigned by analogy from the lipid and carbohydrate force field (21–26) used in this study.

In step 1, the single *E. coli* R1 O6 LPS molecule was constructed by generating each region (lipid A, R1 core, and O6 antigen) and linking them together with proper glycosidic linkages, and phosphorylation (Fig. 1 and Table S1) in CHARMM (28). Initial coordinates of the LPS molecules were assigned using internal coordinate information of common glycosidic torsion angle values and then oriented along the *Z* axis (i.e., the membrane normal). This initial structure was subject to Langevin dynamics with a cylindrical restraint potential to retain the LPS molecule to be cylindrical in shape because the initial structure based on the internal coordinate information was not linearly aligned along the *Z* axis. Twelve sequential Langevin dynamics simulations in total were carried out to reduce the molecular radius (perpendicular to the *Z* axis) starting from 16 Å to 5 Å to avoid the potential bad contacts during the membrane assembly.

In step 2 and step 3, the LPS bilayer components including LPS, ions, and water were built and assembled. 25 single *E. coli* R1 O6 LPSs were initially placed in a 5 × 5 square grid with random rotation around the *Z* axis in one leaflet. The grid spacing was based on an initial surface area of 200 Å^2/LPS. To remove bad contacts, a systematic translation (in the *X* and *Y* directions) and rotation (around the *Z*-direction) rigid-body search for each LPS molecule was performed until the average number of bad contacts per lipid reached a minimum. A bad contact is defined by a distance <2.5 Å between heavy atoms. The lower leaflet of the LPS bilayer was then generated by a 180° rotation of the upper leaflet with respect to the *X* axis. To improve sampling and to check simulation convergence, we made four independent systems for each LPS bilayer using different initial random seed numbers for assembled LPS bilayers. 100 Ca^{2+} ions were added to the LIPA bilayer system and 250 Ca^{2+} ions to the LPS0, LPS5, and LPS10 bilayer systems to neutralize each system; the total charges of each *E. coli* O6 lipid A and R1 core are $-4e$ and $-6e$, respectively, and the O-antigen segment is neutral. 150 mM KCl was used for bulk ionic solution. To obtain initial positions of ions, 2000 steps of Monte Carlo simulations for Ca^{2+}, K^{+}, and Cl^{-} ions were performed, where Ca^{2+} ions were restricted to the lipid A and core region, and K^{+} and Cl^{-} ions to the bulk region. The interaction energies were calculated using a primitive model with the Coulombic interaction scaled by a dielectric constant of 80 and van der Waals interaction. Finally, a water box was sequentially overlaid with a LPS bilayer and ions, starting from phosphate groups of lipid A to make sure that the systems were fully hydrated. Any water molecule whose oxygen atom had a distance <2.2 Å from any LPS heavy atoms or ions was removed after the overlays. The number of atoms in each bilayer system is ~30,000 (LIPA), ~60,000 (LPS0), ~124,000 (LPS5), and ~192,000 (LPS10).

In addition to the homogeneous LPS bilayers, we also constructed four heterogeneous LPS bilayers with various lengths of O-antigens mixed: LPS0/LPS5 with 25% (MIX5_25) and 50% (MIX5_50) of LPS5 and LPS0/LPS10 with 25% (MIX10_25) and 50% (MIX10_50) of LPS10. Again, four replicas for each mixed bilayer were generated independently. For the mixed LPS bilayers, corresponding LPS molecules were randomly picked and placed on the 5 × 5 square grid according to their mixed ratio, followed by the same procedures with the homogeneous LPS bilayer construction. The number of atoms in each bilayer system is ~135,000 (MIX5_25), ~136,000 (MIX5_50), ~160,000 (MIX10_25), and ~162,000 (MIX10_50).

In step 4 and step 5, equilibration and production simulations were performed. About 1-ns equilibration simulations were performed for all the LPS bilayers using CHARMM (28) with the C36 lipid (24,29) and carbohydrate (21–23,25,26) force fields, and a modified TIP3P water model, which is intended for use with the CHARMM force fields (30,31). To assure gradual equilibration of the assembled system, based on equilibration steps used in *Membrane Builder* (32,33) in CHARMM-GUI (34), various restraints were applied to the LPS and water molecules, and the restraint

forces were gradually reduced during the equilibration. Additional dihedral angle restraints were applied to restrain all the sugar rings to the pertinent chair conformation, and these restraints were kept in the production simulations. The NVT (constant particle number, volume, and temperature) dynamics was used first and followed by the NPT (constant particle number, pressure, and temperature) dynamics during the equilibration. After equilibration, a 100-ns NPT production run was performed with NAMD (35) for all the LPS bilayers except LIPA and LPS0 (200-ns production). *XY* dimensions were allowed to vary independently of the *Z*-direction in NPT dynamics. All simulations were performed under the following protocol. We used 2-fs time step with the SHAKE algorithm (36). The van der Waals interactions were smoothly switched off at 10–12 Å by a force-switching function (37) and the long-range electrostatic interactions were calculated using the particle-mesh Ewald (38) method. The temperature and pressure were held at 310.0 K and 1 bar, respectively. In CHARMM simulations, Langevin temperature control was used for NVT dynamics. Temperature and pressure controls were achieved with a Hoover thermostat (39) and Langevin-piston for NPT dynamics (40,41). For NAMD NPT simulations, Langevin dynamics was used to maintain constant temperatures with a Langevin coupling coefficient set to 1 ps^{-1}, and a Nosé-Hoover Langevin-piston (42,43) was used to maintain constant pressure with a piston period of 50 fs and a piston decay of 25 fs.

NMR experiments

NMR experiments were performed on an *E. coli* O6 polysaccharide sample (19 mg) in D_2O solution (0.55 mL), obtained by gel permeation chromatography where it was eluted with a narrow distribution directly after the void volume (27). ^1H NMR chemical shifts were referenced to internal 3-trimethylsilyl-(2,2,3,3-$^2H_4$)-propanoate (TSP, 0.1 mg mL^{-1}, δ_H 0.00) and ^{13}C NMR chemical shifts were referenced to external 1,4-dioxane in D_2O (δ_C 67.40). The temperature was calibrated to 48.0 ± 0.1°C with a neat deuterated methanol sample (44) before all the experiments. The chemical shifts of the ^1H and ^{13}C resonances from the sugar residues in the repeating units of the polysaccharide were predicted by the CASPER program (45,46) and subsequently assigned using $^1H,^{13}C$-HSQC (47), $^1H,^{13}C$-H2BC (48), $^1H,^{13}C$-HMBC (49), and $^1H,^1H$-TOCSY (50) experiments on a 600 MHz Bruker AVANCE III spectrometer equipped with a 5 mm inverse Z-gradient TXI ($^1H/^{13}C/^{31}P$) probe. A ^1H NMR spectrum of the polysaccharide was recorded on a 500 MHz Bruker AVANCE spectrometer equipped with a TCI Z-Gradient Cryoprobe using 128 scans, 64 k data points, a spectral width of 12 ppm, and a recycle delay of 5 s. The free induction decay was zero-filled once and resolution enhancement was obtained by applying a Lorentzian-Gaussian window function (lb = −0.3 Hz and gb = 0.2). A diffusion filtered ^1H NMR experiment (51) was also carried out on the 500 MHz spectrometer using 512 scans, 14k data points, a spectral width of 10 ppm, a diffusion time of 150 ms (Δ), a pulsed field gradient duration of 3.6 ms (δ), and a recycle delay of 10 s.

Phase-sensitive $^1H,^1H$-NOESY experiments (52,53) with calibrated zero-quantum filters (54) were performed on a 700 MHz Bruker AVANCE III spectrometer equipped with a TCI Z-Gradient Cryoprobe. The spectra were recorded with 256 × 16 k points in the F_1 and F_2 dimensions, a spectral width of 6 ppm, and a recycle delay of 10 s. Volumes of crosspeaks and of anomeric diagonal peaks from 13 experiments of different mixing times (35–165 ms) were used to construct NOE buildup curves by the PANIC approach (55), where each crosspeak volume was divided by its anomeric diagonal peak volume at that mixing time. Because the anomeric resonances of residues B and C were overlapping (see Fig. 3 for *residue labels*), an averaged volume of these signals was used for these two residues. Cross-relaxation rates (σ) were calculated by fitting functions of first order to the PANIC data using an in-house-written script in MATLAB (The MathWorks, Natick, MA). Constraints used in the fitting procedure were that the *y*-axis intercept should be within 5% of the value at the longest mixing time (165 ms) and that the coefficient of determination (R^2) should be higher than 0.9. Data points at the longest mixing time were removed until the fitting criteria were fulfilled and a final manual inspection reassured the quality of the fitting procedure. In cases where cross-relaxation rates of a proton pair were extracted from crosspeaks on both sides of the diagonal, the σ-values were averaged. The cross-relaxation rates were used to calculate effective $^1H,^1H$ distances employing the isolated spin pair approximation (56) and a reference distance of 2.34 Å (from the LPS10 simulations, see MD simulations) between the H1 and H3 protons in residue C having an experimentally determined cross-relaxation rate $\sigma = 1.19\ s^{-1}$.

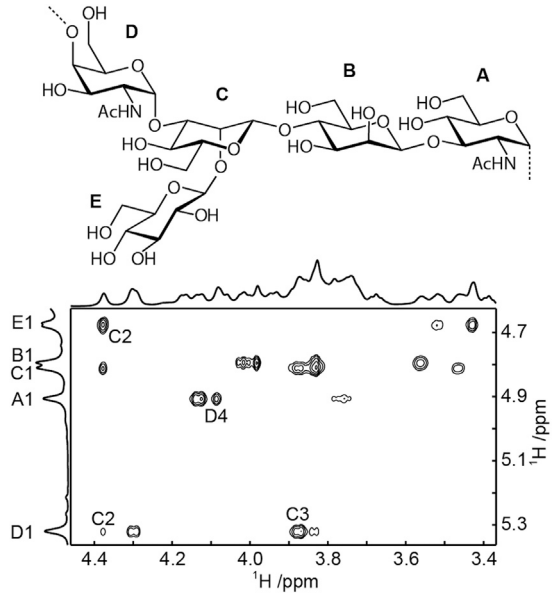

FIGURE 3 Top. A schematic structure of the repeating unit of the O-antigen polysaccharide from *E. coli* O6. Bottom. Part of a $^1H,^1H$-NOESY spectrum (τ_{mix} = 160 ms) with selected O-antigen resonances annotated.

$^1H,^1H$-NOE buildup curves were simulated (57) using SIMMA (58) with dynamics described by the isotropic model-free approach (59–61). The global correlation time (τ_c) was assumed to be 6 ns (62) and other dynamic parameters such as the generalized order parameter (S^2) and the internal correlation times (τ_e) were estimated by fitting simulated curves describing the anomeric autopeak decay to experimental data (57). Possible spin diffusion processes were investigated by simulating NOE buildup curves for proton pairs and removing intervening protons from the calculations to see to what extent the alteration affected the NOE buildup and the cross-relaxation rates. The internuclear distances in the calculations were taken from a representative structure of the LPS10 MD simulation with averaged glycosidic torsion angles close to their highest probable counterparts. The dynamic parameters used in the NOE buildup simulations were set to $\tau_c = 6$ ns, $\tau_e = 0.6$ ns, and $S^2 = 0.7$.

RESULTS AND DISCUSSION

Comparison with NMR experiments

To compare with and validate the structural models in the MD simulations, NMR studies on the O-antigen polysaccharide of *E. coli* O6 using $^1H,^1H$-NOESY experiments were conducted at 48°C, and both ^1H and ^{13}C chemical shift assignments are presented in Table S2. First, the average number of repeating units in the NMR polysaccharide sample is estimated from a ^1H NMR spectrum. A low intensity signal is observed at 5.27 ppm, slightly upfield to the signal of the anomeric proton of residue D (see Fig. 3 for *residue labels*).

The low intensity signal is assumed to be a terminal residue of the polysaccharide (D′) after evaluation of a ^{1}H diffusion filtered NMR spectrum, where the signal at 5.27 ppm has a similar diffusion coefficient as the major polysaccharide signals. In addition, the ^{1}H chemical shifts of the D′ spin system (δ_{C1} = 99.82, δ_{H2}/δ_{C2} = 4.22/50.60, δ_{H3}/δ_{C3} = 4.02/69.73, δ_{H4}/δ_{C4} = 4.02/70.13, and δ_{H5}/δ_{C5} = 4.22/72.56) are consistent with a terminal α-D-Gal*p*NAc residue, as predicted by the CASPER program (45,46). The integral ratio of the signal of the anomeric protons of residues D and D′ in the ^{1}H NMR spectrum shows that the number of polysaccharide repeating units is ~16 on average, i.e., very similar to what have been observed for other *E. coli* O-antigen polysaccharides (63,64).

Thirteen ^{1}H,^{1}H-NOESY experiments with mixing times varying between 35 and 165 ms were performed to provide information of interresidue distances between protons (Fig. 3). Interresidue atom correlations are found between all sequentially linked residues except for the two β-D-mannosyl residues B and C, where separate integrations of crosspeaks are not possible due to spectral overlap in the 2D ^{1}H,^{1}H-NOESY spectra. From NOE buildup curves, cross-relaxation rates (σ) are calculated using the PANIC approach (55) (Fig. 4) and the results are presented in Table 1. The PANIC approach is suitable in this study

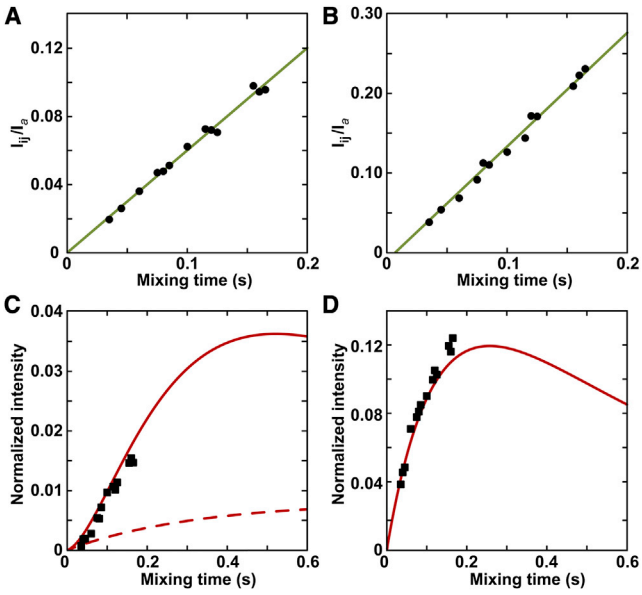

FIGURE 4 (*A*) The PANIC plot of the intraresidue proton pair C1-C3 where the slope of the fitted curve corresponds to $\sigma_{C1\text{-}C3}$. (*B*) The PANIC plot of the interresidue proton pair A1-D4 where the slope of the fitted curve corresponds to $\sigma_{A1\text{-}D4}$. (*C*) Experimental NOE buildup of D1-C1 (*squares*) compared to simulated NOE buildup where the C3 spin has been included (*solid line*) or excluded (*dashed line*) in the calculations. The difference between the two simulated curves shows that spin diffusion through proton C3 is responsible for an enhancement of $\sigma_{D1\text{-}C1}$. (*D*) Experimental NOE buildup of D1-C3 (*squares*) compared to simulated NOE buildup for the same proton pair (*solid line*).

TABLE 1 Intra- and interresidue proton-proton cross-relaxation rates (σ in s^{-1}) from PANIC NOE buildup curves, NOE-based experimental atom distances (r_{NMR} in Å), and calculated atom distances (r_{MD} in Å) from the LPS10 simulation

Proton pair	σ	r_{NMR}	r_{MD}[a]
A1-A2	1.62	2.22	2.43
B1-B2	0.82	2.49	2.43
B1-B5	1.35	2.29	2.36
C1-C2	0.61	2.61	2.47
C1-C3	1.19[b]	2.34	2.34[b]
C1-C5	0.76	2.57	2.36
E1-E3	0.46	2.73	2.47
A1-D4	0.60	2.62	2.20
B1-A3	0.95	2.46	2.24
D1-C3	1.31	2.30	2.28
E1-C2	1.07	2.38	2.46

[a]Standard errors are smaller than 0.01 for all the proton pairs.
[b]Used as a reference in the r_{NMR} calculations.

because the molecular size of our sample reduces the time in which the initial rate limit is valid, which is compensated for in the PANIC approach, thereby allowing longer mixing times to be used in the experiments. The internuclear distances (r_{NMR}) calculated from the cross-relaxation rates are also presented in Table 1 together with the effective distances (r_{MD}) from the MD simulations by using an $\langle r^{-6} \rangle$ averaging over O-antigen repeating units 2–9 for 50 LPS10 molecules, i.e., leaving out the first and the last repeating units to omit end effects. The deviations between r_{NMR} and r_{MD} for intraresidue proton pairs are <0.3 Å. For the interresidue proton-proton crosspeaks of atoms D1-C1, D1-C2, D1-C4, and B5-A3, r_{NMR} appears to be shorter than r_{MD} (up to 1 Å). The lack of agreement can be explained by spin diffusion caused by intervening protons (in these cases C3 and B1) that relays the magnetization, thus enhancing the NOE, resulting in a too short apparent distance between protons. The spin diffusion can be identified by comparing simulated NOE buildup curves based on molecular models with and without the intervening proton (57), where the spin diffusion can enhance the NOE buildup dramatically (Fig. 4). The deviations between r_{NMR} and r_{MD} for the remaining investigated interresidue proton pairs are <0.3 Å, for which a single conformational region is highly preferred (Fig. S2) with a single exception, namely, the A1-D4 distance that differs by 0.42 Å. This could be due to a skewed population distribution between the major and the minor conformational states of the A-D glycosidic torsion angles (Fig. S2), as deduced by the force field-based MD simulation. The experimental NMR data indicates that the minor state (from MD simulations) should be favored instead of the major one. Reminiscent of this discrepancy is that observed for methyl β-maltoside (65) in which an experimentally observed trans-glycosidic proton-proton distance was longer than in the MD simulation, which used a similar force field as in the present case. The overall agreement between MD and NMR data is very encouraging,

despite the differences between the simulation and experimental conditions, such as concentrations and that the NMR experiments were performed on an O-antigen polysaccharide solution instead of LPS in a bilayer.

Structure and dynamics of LPS molecules in a bilayer

To examine the influence of the LPS molecular length on structure and dynamics of LPS molecules in a bilayer, the length of each LPS molecule was first calculated by measuring the molecular dimension along the *Z* axis. The average molecular lengths are 22 ± 0.09 (LIPA), 44 ± 0.05 (LPS0), 102 ± 0.7 (LPS5), and 150 ± 1.0 Å (LPS10) calculated from the last 50 ns. The small standard errors indicate that the LPS molecular length is fairly stable in the course of the LPS bilayer simulations. For comparison, the initial lengths are 21 (LIPA), 45 (LPS0), 89 (LPS5), and 136 Å (LPS10). This basic structural information could serve as an important factor in building reasonable bilayer simulation systems with different lengths of LPS molecules.

Heavy atom density profiles along the bilayer normal (*Z* axis) for the core and O-antigen repeating units 1–5 are shown in Fig. 5 and compared for LPS0, LPS5, and LPS10. The core sugar residues in LPS0 are more extended than the same residues in LPS5 and LPS10, and the same behavior is found for the repeating units 1–5 in LPS5 compared to LPS10. Therefore, having more components in the LPS molecules does have an impact on the LPS structures in a LPS bilayer. It is clear that the terminal sugar residues are more stretched and dynamic due to less packing compared to the ones inside.

As with other lipids, LPS are dynamic in their structure, as shown in Fig. 6, which are seven different LPS10 molecules randomly chosen from the simulations. The time averaged root mean-squared fluctuation (RMSF) is a measure of the relative flexibility and provides a means to assess the relative flexibility of different regions of the molecule. For example, the calculated RMSF for the heavy atoms of LPS5 sugar residues (Fig. S3) reflects that the core sugars show a more pronounced rigidity compared to the O-antigen sugars. This could be related to the fact that the calcium ion coordination network (see below) restricts the motions of the core sugars and thus lowers the dynamics in this region. In contrast, terminal sugar residues are highly flexible, which was also experimentally observed by ^{13}C NMR relaxation studies (62). For each system, the average structure was used as the reference in RMSF calculations, and the starting coordinate was used for structure alignment.

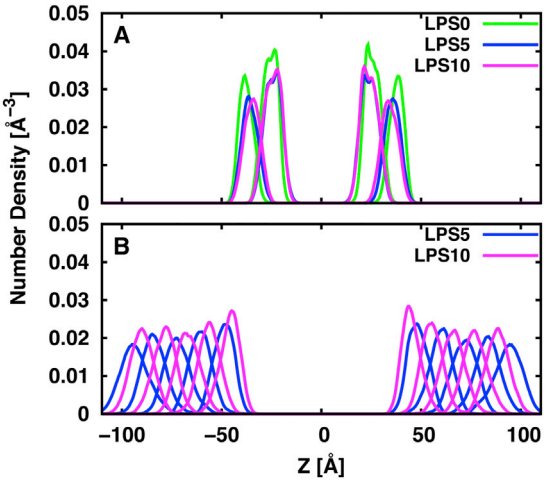

FIGURE 5 Heavy atoms density profiles along the membrane normal (*Z* axis) for (*A*) the inner and outer core and (*B*) O-antigen repeating units 1–5 in the LPS0, LPS5, and LPS10 bilayers. The *Z* axis is truncated to show the core and O-antigen repeating units 1–5 in detail.

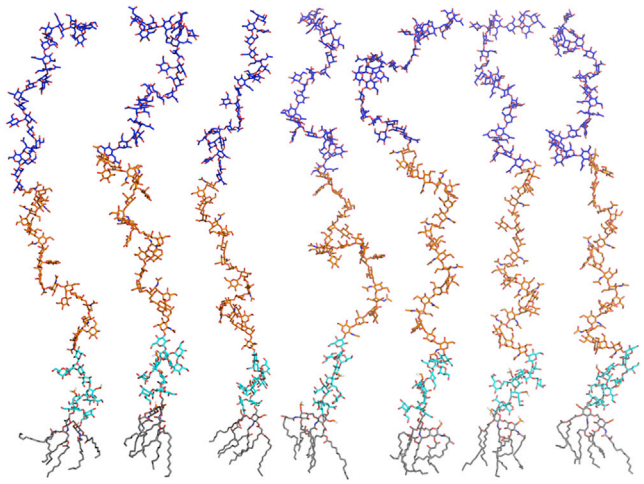

FIGURE 6 Structures of seven different LPS10 molecules that are randomly chosen from the LPS10 bilayer at 100-ns time point. The color scheme is the same as in Fig. 2.

Structure and dynamics of LPS bilayers

To elucidate the effect of LPS molecular length on LPS bilayer properties, per-lipid surface area, hydrophobic thickness, and acyl chain order parameters were calculated and compared between the LIPA, LPS0, LPS5, and LPS10 bilayers.

Fig. S4 plots the time series of per-lipid surface area for four different LPS bilayers. The surface area gives a general idea of lipid packing in the membrane plane. Because of the huge computational cost of the LPS5 and LPS10 systems, the total simulation time of each replica is 100 ns for LPS5 and LPS10, but 200 ns for LIPA and LPS0. Fig. S4 shows the time evolution of the simulations toward an equilibrium state (the last 50 ns of each replica). Lipids with two acyl chains can equilibrate their surface area per lipid relatively fast (<50 ns) (29) due to their ability to quickly translate and internally isomerize in the liquid crystalline state.

The LPS lipids do not show this behavior due to multiple chains and their random rotation (distribution) in different replicas. Although statistically each individual replica of Lipid A (Fig. S4 *A*) is equilibrated, individual simulations show different average areas, which is likely due to their slow lateral diffusion. The initial conditions appear to influence the average area on the 200-ns timescale in these bulky lipids. This is somewhat more pronounced for those with the R1 core and the O6 antigens. Although this shows that multiple runs for ~200 ns are important to give bounds to the surface area per lipid, the standard errors are relatively small, i.e., <2.0 Å^2 (Table 2). These results might indicate a natural variation of per-lipid area of LPS patches in the outer membrane.

Average lipid properties are calculated over the last 50 ns and summarized in Table 2. The average areas per lipid are around 168 Å^2 (LIPA), 180 Å^2 (LPS0), and 190 Å^2 (LPS5/LPS10). Considering the fact that the lipid area in 1,2-dimyristoyl-*sn*-glycero-3-phosphocholine (DMPC) bilayers (having acyl tail length similar to lipid A, but with only two chains) is ~60 Å^2 (66), the lipid area in our simulations, which is about three times larger than that of DMPC, appears to be in a reasonable range. The increasing lipid area (LIPA < LPS0 < LPS5/LPS10) indicates that with the core and O-antigen sugar residues on top of lipid A, the corresponding bilayer tends to expand and has a larger area. A possible reason for the LPS0 bilayers increased surface area compared to the LIPA bilayer might be the stronger electrostatic repulsive interaction due to the additional negative charges in the core region. On the other hand, the O-antigen might be bulkier and tends to take up more space than sugars in the core region, so the steric interactions in the O-antigen region push LPS molecules away from each other, which leads to the increased surface area seen in the LPS5 and LPS10 bilayers compared to the LPS0 bilayer.

The hydrophobic thickness of the LPS bilayers is calculated by measuring the average distance between the acyl chain C2 (only in chain #4 and #6) and C4 carbon atoms (the carbon after carbonyl group) of lipid A in both leaflets (see Fig. 1 *B* for *chain labels*). As shown in Table 2, the average thicknesses are 22.9 (LIPA), 21.6 (LPS0), 20.1 (LPS5), and 20.7 Å (LPS10), respectively, and thus as expected the hydrophobic thickness is inversely proportional to the area per lipid; i.e., the LIPA bilayer has the biggest thickness and the smallest area. Snyder et al. (67) reported that at 20°C the electron density peaks of the lipid A headgroup are at ±21 Å in gel phase by x-ray diffraction experiments, and the repeat period changes by ~5 Å between gel and liquid crystalline phase. The corresponding headgroup peak calculated from our density profile at 310 K is about ±18 Å, which agrees with the experimental values assuming that the repeat period decrease comes from headgroup spacing changes.

Lipid deuterium order parameters (S_{CD}) can be associated with bilayer fluidity. As the order parameter increases, the chain order increases as well. The order parameter of each C-D bond vector is defined as

$$S_{CD} = \frac{1}{2}\langle 3\cos^2\theta_{CH} - 1\rangle, \quad (1)$$

where θ_{CH} is the time-dependent angle between the C-H bond vector and the bilayer normal; the angular bracket denotes a time and ensemble average (68). Lipid order parameters of acyl chain #4 (12 carbons) and #6 (14 carbons) for the LIPA, LPS0, LPS5, and LPS10 bilayers are shown in Fig. 7. A good correlation is observed between the trend of calculated order parameters, lipid area, and hydrophobic thickness. For example, the LIPA bilayer is the most ordered bilayer system with the largest hydrophobic thickness and the smallest surface area. The observed lower acyl chain packing with increasing LPS length is also consistent with experiment study by wide-angle x-ray scattering (69). Acyl chain #4 and #6 are also showing similar trends, indicating that these bilayer systems are well equilibrated considering the similar chemical structures of these two chains. Our simulation also agrees well with the new LPS membrane simulation study with GLYCAM force field by Kirschner et al. (70), indicating that our bilayer structures are reasonable. Compared to the high order parameters (up to ~0.35) obtained in the *E. coli* outer membrane simulation study (including lipid A and the inner core) using GROMOS 53A6 force field by Piggot et al. (71), the order parameters from all four different bilayer simulations are below 0.30 with increasing disorder along the fatty acid chains toward the last methyl groups, showing a better agreement with experimental DMPC order parameters (68) and in correspondence to a liquid crystalline phase.

Ion and water distribution

Individual LPS molecules on the bilayer surface of bacterium are held together by various interactions, such as electrostatic interaction, hydrophobic interactions, and

TABLE 2 Average lipid bilayer properties over the last 50 ns for the homogeneous and heterogeneous LPS bilayers with four independent systems

Systems	LIPA	LPS0	LPS5	LPS10	MIX5_25	MIX5_50	MIX10_25	MIX10_50
Area per lipid (Å^2)	168 (1.4)	180 (1.2)	193 (2.0)	187 (1.1)	186 (1.9)	190 (1.0)	187 (1.2)	186 (1.7)
Hydrophobic Thickness (Å)	22.9 (0.2)	21.6 (0.1)	20.1 (0.2)	20.7 (0.1)	20.9 (0.2)	20.4 (0.1)	20.8 (0.1)	20.9 (0.2)

Standard errors are given in parenthesis.

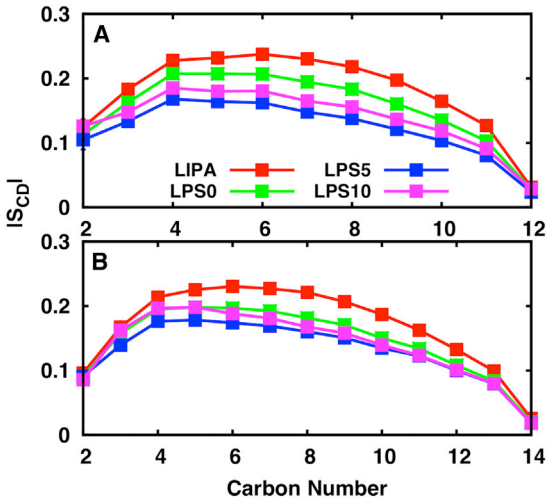

FIGURE 7 Average ^{2}H order parameters for (*A*) chain #4 and (*B*) chain #6 of the LIPA, LPS0, LPS5, and LPS10 bilayers at 310 K (see Fig. 1 *B* for *acyl chain number*; standard errors over 4 replicas are smaller than 0.02 for all the data points).

hydrogen bonds (72). It is well known that divalent cations intercalated between LPS molecules are crucial for maintaining the integrity of the outer membrane structures, as they prevent repulsion between the negatively charged groups of adjacent LPS molecules (1,73). Chelating agents that are able to bind divalent cations (e.g., EDTA) can cause destabilization of the outer membrane and increase susceptibility of antibiotics to the bacteria (74).

Fig. S5 shows the density profiles of Ca^{2+} ions, phosphate, and carboxylate groups attached to sugars (Fig. 1 *A*) along the *Z* axis in the LIPA, LPS0, LPS5, and LPS10 bilayers. The phosphate distribution is split into two regions in LPS0, LPS5, and LPS10 systems, which correspond to the lipid A headgroup and the inner core sugar residues, respectively. Calcium ions have a similar and broader distribution because the carboxyl groups fill the gap between the two peaks. This feature indicates that calcium ions closely interact with both phosphate groups and carboxylate groups, which was also observed in the simulations by Lin and Straatsma (75). In addition to the phosphate and carboxylate groups, other potential ligands for calcium ion are hydroxyl oxygen atoms and water molecules. Coordination composition of Ca^{2+} (Table S3) based on the integral of the radial distribution function shows no significant difference between the LIPA, LPS0, LPS5, and LPS10 bilayers. As the bilayer area increases from LIPA to LPS5/LPS10, phosphate contribution slightly decreases and water contribution slightly increases. It is possible that multiple oxygen atoms from the same phosphate group can coordinate a Ca^{2+} ion, because the radial distribution function was calculated between Ca^{2+} ions and oxygen atoms; however, this scenario occurred less frequently (~25% of the cases). During the simulations, calcium ions are predominantly hexacoordinated (i.e., summation of individual contribution to the coordination number is ~6), which agrees with the calcium ion coordination number measured by x-ray diffraction in $CaCl_2$ aqueous solutions (76). It should be pointed out that >50% of the calcium ion coordination sites are taken up by water molecules, showing that even though calcium ions bind strongly to the LPS molecules, they still remain well hydrated. It also reflects that water molecules play a very important role in stabilizing calcium ion and the LPS bilayer. Fig. S6 shows a calcium ion coordination site in the LPS0 bilayer between two adjacent LPS0 molecules, where the calcium ion is coordinated with two phosphate groups from neighboring LPS molecules, one carboxylate group, and three water molecules.

Because the lipid composition of a particular membrane plays a key role in water permeability, water density profiles along the *Z* axis are shown in Fig. 8 to compare the differences in three LPS bilayers and also with a DMPC bilayer. In all the LPS systems, water molecules pass the inner core region and penetrate deep into the hydrophobic core region, which agrees well with another simulation study (70) and neutron scattering measurements (77,78) for smooth LPS (containing O-antigen) (79) bilayers from *Pseudomonas aeruginosa* in the liquid crystalline phase. Clearly, the core and O-antigen sugars are well hydrated in our simulations. In addition, water penetration shows no remarkable difference between the LPS0, LPS5, and LPS10 bilayers. The penetration depth is also very similar between LPS and DMPC bilayers. The reason could be that the core and O-antigen sugar residues provide a hydrophilic barrier that apparently protects against hydrophobic molecules

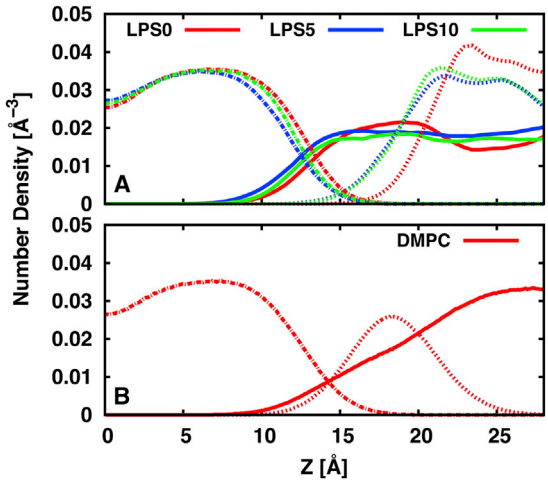

FIGURE 8 (*A*) Density profiles of water molecule (*solid line*), inner core (*dotted line*), and lipid tail (*dashed line*) heavy atoms along the *Z* axis in the LPS0, LPS5, and LPS10 bilayers. The *Z* axis is truncated to show the water distribution around the inner core region in detail. (*B*) Density profiles of water molecule (*solid line*), lipid headgroup (*dotted line*), and carbon tail (*dashed line*) in the DMPC bilayers. The DMPC data is from Klauda et al (29).

(14), but it does not prevent the rapid diffusion of small polar molecules, like water molecules. This is also why Gram-negative bacteria are generally more resistant to hydrophobic antibiotics and detergents than their Gram-positive counterparts. The hydrophilic polysaccharide component is responsible for the exclusion of hydrophobic molecules and the hydrophobic lipid A of LPS limits the entry of hydrophilic compounds (80).

Another indicator of LPS dynamics is the permeability of ions. Unlike calcium ions, which are mostly immobilized in the lipid A headgroup and inner core regions, potassium and chloride ions are very mobile in most cases (Fig. S7) unless they are stuck with their counter-ions, i.e., phosphate groups for potassium ions and calcium ions for chloride ions. They can travel up and down along the *Z*-direction, sometimes from bulk solution all the way into the core region in the present simulation timescale. Some of the potassium ions penetrate very deep and even interact with the headgroup of lipid A in the LPS0 bilayers. At the same time, having more polysaccharides hinders the ion permeability. Fewer ions were observed in the core region in the LPS5 and LPS10 bilayers compared to the LPS0 bilayer, although this might change over time. Interestingly, in the LPS0 bilayers, more potassium ions penetrate inside the bilayer than chloride ions, but in LPS5 and LPS10 bilayers, it is opposite. This might arise from the fact that in the LPS0 bilayers, potassium ions can associate with the ester groups, but they may interact too tightly with sugar residues in the O-antigen region in the LPS5 and LPS10 bilayers, compared to chloride ions.

Heterogeneous LPS bilayer

Heterogeneous LPS bilayers are biologically more relevant (72), considering various lengths of the O-antigen repeating units. Mixed LPS bilayer simulations allow us to validate the findings from the homogenous LPS bilayer simulations and also, more importantly, allow us to further investigate the impact of the O-antigen chain length heterogeneity on the LPS molecular structure and dynamics in a bilayer, and also on the bilayer properties.

The distances between the lipid A phosphate groups and the first residue of each O-antigen repeating unit along the *Z* axis are shown in Fig. 9, *A* and *B*, and compared between the 25%, 50%, 100% of LPS5 and LPS10 bilayers. Clearly, the LPS conformation is highly dependent on its local environment. The O-antigen conformations of LPS5/LPS10 in higher concentration tend to be more extended. The average tilt angle of each repeating unit shows that the O-antigen of LPS5 and LPS10 molecules tend to tilt more from the *Z* axis when its concentration is low (Fig. 9, *C* and *D*). Because the glycosidic torsion angles are quite well defined (Fig. S2) and maintain similar values in the heterogeneous LPS bilayer simulations, the difference between the O-antigen conformations at a different concentration might come from a polymeric effect due to the large number of small glycosidic

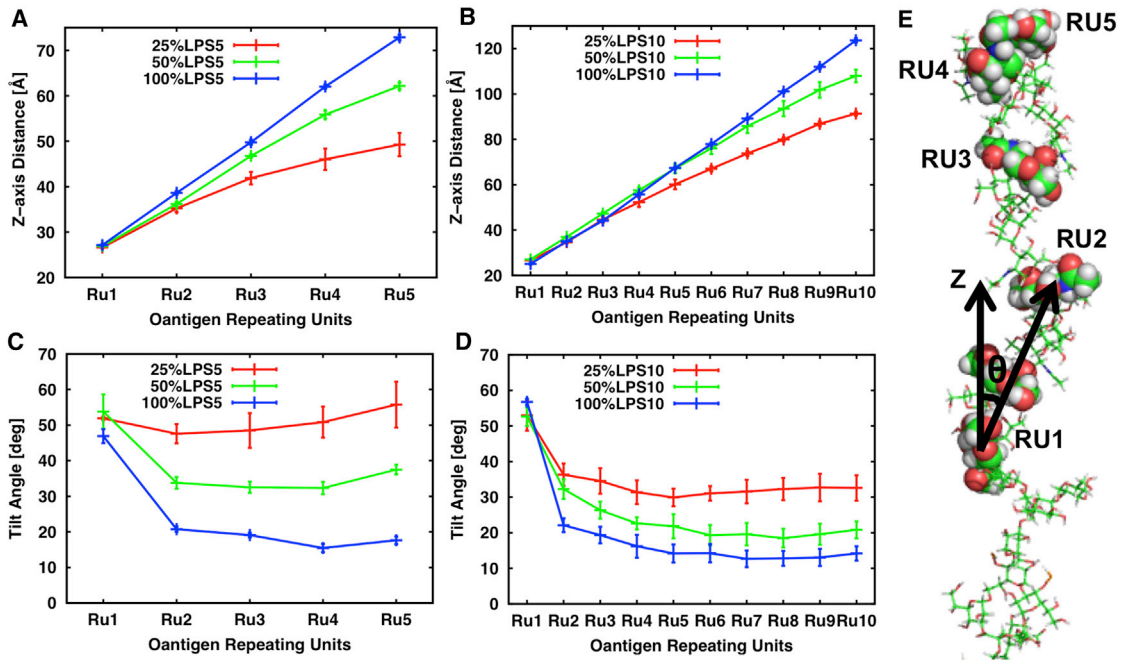

FIGURE 9 Average distances (with standard errors over 4 independent simulations) between the lipid A phosphate groups and the first residue of each O-antigen repeating unit along the *Z* axis in the heterogeneous and homogeneous (*A*) LPS5 and (*B*) LPS10 bilayers. Average tilt angles (with standard errors) of each repeating unit in the heterogeneous and homogeneous (*C*) LPS5 and (*D*) LPS10 bilayers. (*E*) The tilt angle is defined by the vector made by the first residue of repeating unit 1 and the last residue of each repeating with respect to the bilayer normal (*Z* axis).

torsion angles changes in the O-antigen region. As the concentration of the LPS5/LPS10 molecules decrease, the O-antigen sugars of the LPS molecules experience less support from adjacent molecules and are free to bend further. In addition, the comparison of RMSF indicates that the LPS5 and LPS10 molecules show a much higher fluctuation or increased dynamics, when their concentrations are lower, meaning that the LPS molecules are more flexible when the packing is less compact (Fig. S8). However, there is no obvious difference between LPS0 dynamics in different O-antigen concentrations due to the dense packing (in the core region) and the stabilization from the calcium coordination network.

Table 2 reports key lipid bilayer properties (i.e., surface area per lipid and hydrophobic thickness) for four heterogeneous LPS bilayer systems: MIX5_25, MIX5_50, MIX10_25, and MIX10_50. Consistent with the homogeneous LPS simulations, we found that having O-antigen sugar residues does have an impact on the lipid surface area and other lipid properties. Increased surface area was found even in the lowest O-antigen concentration (25%) of the LPS5 and LPS10 mixed bilayers. We also noticed that the concentration of the component lipid molecules does not have a significant or consistent effect on bilayer properties in LPS5 and LPS10 mixed bilayers, and the differences of per-lipid area and hydrophobic thickness between the corresponding 25% and 50% mixed bilayers are not substantial. Therefore, bilayer properties might be determined by more factors. Besides LPS composition, the distribution of LPS molecules of different O-antigen chain lengths is also an important contributor to the heterogeneous bilayer properties, which makes the situation more complicated.

CONCLUSIONS

Lipopolysaccharide is an amphipathic glycolipid that is only found in the outer membrane of Gram-negative bacteria and appears to be a major contributor to the permeability barrier in these organisms (81,82). In this work, we used MD simulations of four LPS bilayers composed of *E. coli* R1 O6 LPS molecules of various lengths to demonstrate the effect of LPS molecular length on the structure and dynamics of LPS molecules in a bilayer, and also on LPS bilayer properties. Furthermore, NMR studies on the O-antigen conformation using ^{1}H,^{1}H-NOESY experiments were carried out to compare with and validate the MD simulations. Overall, good agreement is observed between effective interproton distances derived from the NMR experiments on the O-antigen polysaccharide in solution and those calculated from the MD simulations of the LPS anchored in the membrane, thereby giving support to the present simulations.

Our study shows that the addition of LPS components (core and O-antigen repeating units) does have an influence on both LPS molecular structure and its overall bilayer properties. For LPS structure, the terminal sugar residues are always more flexible and extended compared to the sugars buried deeper or closer to the membrane. The sugar residues in the core region of the membrane are more rigid with less fluctuation compared to O-antigen sugar residues, and its rigidity arises from the nature of the calcium-mediated, cross-linking electrostatic interaction network. For LPS bilayer properties, the area per lipid increases and bilayer order decreases as more LPS molecular components are added, indicating a looser packing of the LPS molecules in the lipid A region in the smooth LPS (containing O-antigen) membrane with respect to the rough LPS (lacking O-antigen) (79) one. The amount of the O-antigen repeating units does not have a significant impact on bilayer properties, but the varying distribution of LPS molecules between simulation runs might lead to some variations. Having the core and O-antigen sugars on top of lipid A appears to have an impact on LPS bilayer properties; therefore, depending on the scope of the study, it may be wise to consider these effects.

We also evaluated the impact of the O-antigen chain length heterogeneity by simulating four mixed LPS0/LPS5 and LPS0/LPS10 bilayers with a different O-antigen concentration. The LPS molecules tend to be in a more extended conformation at higher concentration of LPS5/LPS10. When the concentration is low, LPS molecules experience less support from adjacent O6 repeating units and tilt more from the Z axis. At the same time, the LPS5 and LPS10 molecules also exhibit greater degrees of mobility and increased dynamics in the heterogeneous bilayer compared with their corresponding homogeneous bilayers.

Our study further shows that >50% of the coordination sites of calcium ions contain neighboring water molecules, which indicates the importance of water molecules to stabilize and maintain the integrity of the bilayer structure. We also identify that water molecules are able to penetrate inside the inner core region in all of the bilayer systems, which is another indication that the sugar residues in the core and O-antigen region are fully hydrated and the hydrophilic polysaccharide component is mainly responsible for the exclusion of hydrophobic molecules. The information gained from this study should be beneficial in future studies exploring the interaction between the bacterial outer membrane and antibiotic drugs.

SUPPORTING MATERIAL

Three tables, eight figures and additional supporting information within a zipped .tar file are available at http://www.biophysj.org/biophysj/supplemental/S0006-3495(13)00874-6.

The authors gratefully acknowledge helpful discussions with Dr. Scott E. Feller, Dr. Alexander D. MacKerell Jr., and Sairam S. Mallajosyula.

This work was supported in part by NSF MCB-1157677, NSF ABI-1145987, HFSP RGP0064/2011, TeraGrid/XSEDE resources (TG-MCB070009) (to W.I.), the National Institute of Supercomputing and Networking/Korea Institute of Science and Technology Information with

supercomputing resources including technical support [KSC-2012-C3-30] (to M.S.Y.), and grants from the Swedish Research Council, the Stockholm Center for Biomembrane Research/Swedish Foundation for Strategic Research and The Knut and Alice Wallenberg Foundation (to G.W.).

REFERENCES

1. Ruiz, N., D. Kahne, and T. J. Silhavy. 2006. Advances in understanding bacterial outer-membrane biogenesis. *Nat. Rev. Microbiol.* 4:57–66.
2. Van Wielink, J. E., and J. A. Duine. 1990. How big is the periplasmic space? *Trends Biochem. Sci.* 15:136–137.
3. Smit, J., Y. Kamio, and H. Nikaido. 1975. Outer membrane of *Salmonella typhimurium*: chemical analysis and freeze-fracture studies with lipopolysaccharide mutants. *J. Bacteriol.* 124:942–958.
4. Brade, H., O. M. Steven, …, M. C. David. 1999. Endotoxin in Health and Disease. Marcel Dekker, New York.
5. Silipo, A., D. C. Castro, …, A. Molinaro. 2010. Lipopolysaccharides. *In* Prokaryotic cell wall compounds. H. K€onig, H. Claus, and A. Varma, editors. Springer-Verlag, Berlin, pp. 133–153.
6. Wang, X., and P. J. Quinn. 2010. Endotoxins: lipopolysaccharides of gram-negative bacteria. *In* Endotoxins: Structure, Function and Recognition, Subcellular Biochemistry. X. Wang and P. J. Quinn, editors. Springer Science+Business Media B.V., Dordrecht, pp. 3–25.
7. Yuriy, K. A., and V. A. Miguel. 2011. Bacterial Polysaccharides: Structure, Chemical Synthesis, Biogenesis and Interaction with Host Cells. Springer-Verlag, Wien.
8. Kamio, Y., and H. Nikaido. 1976. Outer membrane of *Salmonella typhimurium*: accessibility of phospholipid head groups to phospholipase c and cyanogen bromide activated dextran in the external medium. *Biochemistry.* 15:2561–2570.
9. Jiang, X. Q., M. A. Payne, …, P. E. Klebba. 1997. Ligand-specific opening of a gated-porin channel in the outer membrane of living bacteria. *Science.* 276:1261–1264.
10. Ruiz, N., D. Kahne, and T. J. Silhavy. 2009. Transport of lipopolysaccharide across the cell envelope: the long road of discovery. *Nat. Rev. Microbiol.* 7:677–683.
11. Erridge, C., E. Bennett-Guerrero, and I. R. Poxton. 2002. Structure and function of lipopolysaccharides. *Microbes Infect.* 4:837–851.
12. Raetz, C. R. H., and C. Whitfield. 2002. Lipopolysaccharide endotoxins. *Annu. Rev. Biochem.* 71:635–700.
13. Akira, S., S. Uematsu, and O. Takeuchi. 2006. Pathogen recognition and innate immunity. *Cell.* 124:783–801.
14. Esko J.D., T.L. Doering, and C. R. H. Raetz. 2009. Eubacyeria and Archaea. *In* Essentials of Glycobiology. A. Varki, R.D. Cummings, …, M.E. Etzler, editors. Cold Spring Harbor, NY.
15. Pontes, F. J. S., V. H. Rusu, …, R. D. Lins. 2012. The effect of temperature, cations, and number of acyl chains on the lamellar to nonlamellar transition in lipid-A membranes: a microscopic view. *J. Chem. Theory Comput.* 8:3830–3838.
16. Rietschel, E. T., T. Kirikae, …, H. Brade. 1994. Bacterial endotoxin: molecular relationships of structure to activity and function. *FASEB J.* 8:217–225.
17. Stenutz, R., A. Weintraub, and G. Widmalm. 2006. The structures of *Escherichia coli* O-polysaccharide antigens. *FEMS Microbiol. Rev.* 30:382–403.
18. Rietschel, E. T., T. Kirikae, …, U. Zähringer. 1993. The chemical structure of bacterial endotoxin in relation to bioactivity. *Immunobiology.* 187:169–190.
19. Grozdanov, L., U. Zähringer, …, U. Dobrindt. 2002. A single nucleotide exchange in the wzy gene is responsible for the semirough O6 lipopolysaccharide phenotype and serum sensitivity of Escherichia coli strain Nissle 1917. *J. Bacteriol.* 184:5912–5925.
20. Xu, H., A. E. Murdaugh, …, M. E. Núñez. 2013. Characterizing pilus-mediated adhesion of biofilm-forming *E. coli* to chemically diverse surfaces using atomic force microscopy. *Langmuir.* 29:3000–3011.
21. Guvench, O., S. N. Greene, …, A. D. Mackerell, Jr. 2008. Additive empirical force field for hexopyranose monosaccharides. *J. Comput. Chem.* 29:2543–2564.
22. Hatcher, E., O. Guvench, and A. D. Mackerell, Jr. 2009. CHARMM additive all-atom force field for aldopentofuranoses, methyl-aldopentofuranosides, and fructofuranose. *J. Phys. Chem. B.* 113:12466–12476.
23. Guvench, O., E. R. Hatcher, …, A. D. Mackerell, Jr. 2009. CHARMM additive all-atom force field for glycosidic linkages between hexopyranoses. *J. Chem. Theory Comput.* 5:2353–2370.
24. Pastor, R. W., and A. D. Mackerell, Jr. 2011. Development of the CHARMM force field for lipids. *J Phys Chem Lett.* 2:1526–1532.
25. Guvench, O., S. S. Mallajosyula, …, A. D. Mackerell, Jr. 2011. CHARMM additive all-atom force field for carbohydrate derivatives and its utility in polysaccharide and carbohydrate-protein modeling. *J. Chem. Theory Comput.* 7:3162–3180.
26. Mallajosyula, S. S., O. Guvench, …, A. D. Mackerell, Jr. 2012. CHARMM additive all-atom force field for phosphate and sulfate linked to carbohydrates. *J. Chem. Theory Comput.* 8:759–776.
27. Jansson, P. E., B. Lindberg, …, S. B. Svenson. 1984. Structural studies of the *Escherichia coli* O-antigen 6. *Carbohydr. Res.* 131:277–283.
28. Brooks, B. R., C. L. Brooks, 3rd, …, M. Karplus. 2009. CHARMM: the biomolecular simulation program. *J. Comput. Chem.* 30:1545–1614.
29. Klauda, J. B., R. M. Venable, …, R. W. Pastor. 2010. Update of the CHARMM all-atom additive force field for lipids: validation on six lipid types. *J. Phys. Chem. B.* 114:7830–7843.
30. Jorgensen, W. L., J. Chandrasekhar, …, M. L. Klein. 1983. Comparison of simple potential functions for simulating liquid water. *J. Chem. Phys.* 79:926–935.
31. Durell, S. R., B. R. Brooks, and A. Bennaim. 1994. Solvent-induced forces between 2 hydrophilic groups. *J. Phys. Chem.* 98:2198–2202.
32. Jo, S., T. Kim, and W. Im. 2007. Automated builder and database of protein/membrane complexes for molecular dynamics simulations. *PLoS ONE.* 2:e880.
33. Jo, S., J. B. Lim, …, W. Im. 2009. CHARMM-GUI Membrane Builder for mixed bilayers and its application to yeast membranes. *Biophys. J.* 97:50–58.
34. Jo, S., T. Kim, …, W. Im. 2008. CHARMM-GUI: a web-based graphical user interface for CHARMM. *J. Comput. Chem.* 29:1859–1865.
35. Phillips, J. C., R. Braun, …, K. Schulten. 2005. Scalable molecular dynamics with NAMD. *J. Comput. Chem.* 26:1781–1802.
36. Ryckaert, J. P., G. Ciccotti, and H. J. C. Berendsen. 1977. Numerical-integration of Cartesian equations of motion of a system with constraints - molecular-dynamics of N-alkanes. *J. Comput. Phys.* 23:327–341.
37. Steinbach, P. J., and B. R. Brooks. 1994. New spherical-cutoff methods for long-range forces in macromolecular simulation. *J. Comput. Chem.* 15:667–683.
38. Essmann, U., L. Perera, …, L. G. Pedersen. 1995. A smooth particle mesh Ewald method. *J. Chem. Phys.* 103:8577–8593.
39. Hoover, W. G. 1985. Canonical dynamics: equilibrium phase-space distributions. *Phys. Rev. A.* 31:1695–1697.
40. Nose, S., and M. L. Klein. 1983. A study of solid and liquid carbon tetrafluoride using the constant pressure molecular-dynamics technique. *J. Chem. Phys.* 78:6928–6939.
41. Andersen, H. C. 1980. Molecular-dynamics simulations at constant pressure and-or temperature. *J. Chem. Phys.* 72:2384–2393.
42. Feller, S. E., Y. H. Zhang, …, B. R. Brooks. 1995. Constant-pressure molecular-dynamics simulation - the Langevin piston method. *J. Chem. Phys.* 103:4613–4621.
43. Martyna, G. J., D. J. Tobias, and M. L. Klein. 1994. Constant-pressure molecular-dynamics algorithms. *J. Chem. Phys.* 101:4177–4189.

44. Findeisen, M., T. Brand, and S. Berger. 2007. A ^{1}H-NMR thermometer suitable for cryoprobes. *Magn. Reson. Chem.* 45:175–178.

45. Jansson, P.-E., R. Stenutz, and G. Widmalm. 2006. Sequence determination of oligosaccharides and regular polysaccharides using NMR spectroscopy and a novel Web-based version of the computer program CASPER. *Carbohydr. Res.* 341:1003–1010.

46. Roslund, M. U., E. Säwén, …, G. Widmalm. 2011. Complete ^{1}H and ^{13}C NMR chemical shift assignments of mono-, di-, and trisaccharides as basis for NMR chemical shift predictions of polysaccharides using the computer program CASPER. *Carbohydr. Res.* 346:1311–1319.

47. Schleucher, J., M. Schwendinger, …, C. Griesinger. 1994. A general enhancement scheme in heteronuclear multidimensional NMR employing pulsed field gradients. *J. Biomol. NMR.* 4:301–306.

48. Nyberg, N. T., J. Ø. Duus, and O. W. Sørensen. 2005. Heteronuclear two-bond correlation: suppressing heteronuclear three-bond or higher NMR correlations while enhancing two-bond correlations even for vanishing $^{2}J_{CH}$. *J. Am. Chem. Soc.* 127:6154–6155.

49. Bax, A., and M. F. Summers. 1986. ^{1}H and ^{13}C assignments from sensitivity-enhanced detection of heteronuclear multiple-bond connectivity by 2D multiple quantum NMR. *J. Am. Chem. Soc.* 108:2093–2094.

50. Bax, A., and D. G. Davis. 1985. MLEV-17-based two-dimensional homonuclear magnetization transfer spectroscopy. *J. Magn. Reson.* 65:355–360.

51. Wu, D., A. Chen, and C. S. Johnson, Jr. 1995. An improved diffusion-ordered spectroscopy experiment incorporating bipolar-gradient pulses. *J. Magn. Reson. Ser. A.* 115:260–264.

52. Jeener, J., B. H. Meier, …, R. R. Ernst. 1979. Investigation of exchange processes by two-dimensional NMR spectroscopy. *J. Chem. Phys.* 71:4546–4553.

53. Wagner, R., and S. Berger. 1996. Gradient-selected NOESY - a fourfold reduction of the measurement time for the NOESY experiment. *J. Magn. Reson. Ser. A.* 123:119–121.

54. Thrippleton, M. J., and J. Keeler. 2003. Elimination of zero-quantum interference in two-dimensional NMR spectra. *Angew. Chem. Int. Ed. Engl.* 42:3938–3941.

55. Macura, S., B. T. Farmer, and L. R. Brown. 1986. An improved method for the determination of cross-relaxation rates from NOE data. *J. Magn. Reson.* 70:493–499.

56. Thomas, P. D., V. J. Basus, and T. L. James. 1991. Protein solution structure determination using distances from two-dimensional nuclear Overhauser effect experiments: effect of approximations on the accuracy of derived structures. *Proc. Natl. Acad. Sci. USA.* 88:1237–1241.

57. Widmalm, G., R. A. Byrd, and W. Egan. 1992. A conformational study of α-L-Rha*p*-(1→2)-α-L-Rha*p*-(1→OMe) by NMR nuclear Overhauser effect spectroscopy (NOESY) and molecular dynamics calculations. *Carbohydr. Res.* 229:195–211.

58. Eklund, R., K. Lycknert, …, G. Widmalm. 2005. A conformational dynamics study of α-L-Rha*p*-(1→2)[α-L-Rha*p*-(1→3)]-α-L-Rha*p*-OMe in solution by NMR experiments and molecular simulations. *J. Phys. Chem. B.* 109:19936–19945.

59. Lipari, G., and A. Szabo. 1982. Model-free approach to the interpretation of nuclear magnetic-resonance relaxation in macromolecules. 1. Theory and range of validity. *J. Am. Chem. Soc.* 104:4546–4559.

60. Lipari, G., and A. Szabo. 1982. Model-free approach to the interpretation of nuclear magnetic-resonance relaxation in macromolecules. 2. Analysis of experimental results. *J. Am. Chem. Soc.* 104:4559–4570.

61. Palmer, 3rd, A. G. 2004. NMR characterization of the dynamics of biomacromolecules. *Chem. Rev.* 104:3623–3640.

62. Lycknert, K., and G. Widmalm. 2004. Dynamics of the *Escherichia coli* O91 O-antigen polysaccharide in solution as studied by carbon-13 NMR relaxation. *Biomacromolecules.* 5:1015–1020.

63. Larsson, E. A., F. Urbina, …, G. Widmalm. 2004. Structural and immunochemical relationship between the O-antigenic polysaccharides from the enteroaggregative *Escherichia coli* strain 396/C-1 and *Escherichia coli* O126. *Carbohydr. Res.* 339:1491–1496.

64. Svensson, M. V., A. Weintraub, and G. Widmalm. 2011. Structural elucidation of the O-antigenic polysaccharide from *Escherichia coli* O175. *Carbohydr. Res.* 346:449–453.

65. Hatcher, E., E. Säwén, …, A. D. MacKerell, Jr. 2011. Conformational properties of methyl β-maltoside and methyl α- and β-cellobioside disaccharides. *J. Phys. Chem. B.* 115:597–608.

66. Klauda, J. B., N. Kucerka, …, J. F. Nagle. 2006. Simulation-based methods for interpreting x-ray data from lipid bilayers. *Biophys. J.* 90:2796–2807.

67. Snyder, S., D. Kim, and T. J. McIntosh. 1999. Lipopolysaccharide bilayer structure: effect of chemotype, core mutations, divalent cations, and temperature. *Biochemistry.* 38:10758–10767.

68. Vermeer, L. S., B. L. de Groot, …, J. Czaplicki. 2007. Acyl chain order parameter profiles in phospholipid bilayers: computation from molecular dynamics simulations and comparison with ^{2}H NMR experiments. *Eur. Biophys. J.* 36:919–931.

69. Brandenburg, K., S. S. Funari, …, U. Seydel. 1999. Investigation into the acyl chain packing of endotoxins and phospholipids under near physiological conditions by WAXS and FTIR spectroscopy. *J. Struct. Biol.* 128:175–186.

70. Kirschner, K. N., R. D. Lins, …, T. A. Soares. 2012. A glycam-based force field for simulations of lipopolysaccharide membranes: parametrization and validation. *J. Chem. Theory Comput.* 8:4719–4731.

71. Piggot, T. J., D. A. Holdbrook, and S. Khalid. 2011. Electroporation of the *E. coli* and *S. aureus* membranes: molecular dynamics simulations of complex bacterial membranes. *J. Phys. Chem. B.* 115:13381–13388.

72. Kotra, L. P., D. Golemi, …, S. Mobashery. 1999. Dynamics of the lipopolysaccharide assembly on the surface of *Escherichia coli*. *J. Am. Chem. Soc.* 121:8707–8711.

73. Nikaido, H. 2003. Molecular basis of bacterial outer membrane permeability revisited. *Microbiol. Mol. Biol. Rev.* 67:593–656.

74. Edrington, T. C., E. Kintz, …, L. K. Tamm. 2011. Structural basis for the interaction of lipopolysaccharide with outer membrane protein H (OprH) from *Pseudomonas aeruginosa*. *J. Biol. Chem.* 286:39211–39223.

75. Lins, R. D., and T. P. Straatsma. 2001. Computer simulation of the rough lipopolysaccharide membrane of *Pseudomonas aeruginosa*. *Biophys. J.* 81:1037–1046.

76. Licheri, G., G. Piccaluga, and G. Pinna. 1976. X-ray-diffraction study of average solute species in $CaCl_2$ aqueous-solutions. *J. Chem. Phys.* 64:2437–2441.

77. Abraham, T., S. R. Schooling, …, J. Katsaras. 2007. Neutron diffraction study of *Pseudomonas aeruginosa* lipopolysaccharide bilayers. *J. Phys. Chem. B.* 111:2477–2483.

78. Kucerka, N., E. Papp-Szabo, …, J. Katsaras. 2008. Effect of cations on the structure of bilayers formed by lipopolysaccharides isolated from *Pseudomonas aeruginosa* PAO1. *J. Phys. Chem. B.* 112:8057–8062.

79. Osborn, M. J. 1969. Structure and biosynthesis of the bacterial cell wall. *Annu. Rev. Biochem.* 38:501–538.

80. Ni, Y., and R. R. Chen. 2004. Accelerating whole-cell biocatalysis by reducing outer membrane permeability barrier. *Biotechnol. Bioeng.* 87:804–811.

81. Schindler, M., M. J. Osborn, and D. E. Koppel. 1980. Lateral mobility in reconstituted membranes—comparisons with diffusion in polymers. *Nature.* 283:346–350.

82. Leive, L. 1974. The barrier function of the gram-negative envelope. *Ann. N. Y. Acad. Sci.* 235:109–129.

83. Appelmelk, B. J., Y. Q. An, …, J. de Graaf. 1994. Frequencies of lipopolysaccharide core types in *Escherichia coli* strains from bacteraemic patients. *Microbiology.* 140:1119–1124.